# On the Aerodynamic-Noise Sources in a Circular Cylinder Coated with Porous Materials

Zamponi, R.; Avallone, F.; Ragni, D.; van der Zwaag, S.

**DOI**
10.2514/6.2022-3042

**Publication date**
2022

**Document Version**
Final published version

**Published in**
28th AIAA/CEAS Aeroacoustics 2022 Conference

Aeroacoustics Conferences
June 14-17, 2022, Southampton, UK
28th AIAA/CEAS Aeroacoustics 2022 Conference

10.2514/6.2022-3042



# On the Aerodynamic-Noise Sources in a Circular Cylinder Coated with Porous Materials

Riccardo Zamponi*, Francesco Avallone†, Daniele Ragni‡, and Sybrand van der Zwaag§
*Delft University of Technology, Delft, 2629HS, The Netherlands*

**Coating a circular cylinder with porous materials constitutes an effective passive strategy for reducing the flow-induced noise linked to the vortex shedding. Despite the number of investigations in the last decade, the noise-mitigation mechanisms associated with this technique remain unclear. The present research aims to clarify the role played by the alterations in the flow field due to porosity in the aerodynamic-sound attenuation of a cylinder coated with metal foam. Far-field acoustic and particle-image-velocimetry (PIV) measurements were performed at the Delft University of Technology for Reynolds numbers ranging in the subcritical regime. The aeroacoustic results show that a significant tonal and broadband suppression could be achieved with the porous treatment of the body. For the coated cylinder, the dominant sources do not appear to be distributed over the surface but rather are situated several diameters downstream of it, with a lower amplitude. The PIV data reveal that the main effect of the coating is to stabilize the cylinder wake, which results in an elongation of the vortex-formation length and a decrease in the turbulence kinetic energy. In particular, the position where the vortex shedding starts corresponds to the region of the dominant noise sources. The conclusions drawn in this study potentially provide an insightful indication for the design of more effective sound-control solutions.**



## I. Introduction

The aerodynamic noise produced by a circular cylinder immersed in a flow, commonly denoted as Aeolian tone, represents a critical problem involving a large number of engineering applications, including landing-gear systems and high-speed trains. The acoustic sound power level of the noise generated aerodynamically is proportional to the sixth to the eighth power of the flow speed, resulting in a significant increase in sound emissions with a relatively small increase in velocity. From a physical perspective, this source of noise is associated with the shedding of vortical structures that periodically detach from opposite sides of the cylinder surface, forming the von Kármán street.

Given the relevance of the turbulence characteristics in the cylinder wake to the radiated noise, multiple efforts have been devoted to reducing the Aeolian tone using flow-control methods. One of the most promising passive strategies that have been proposed is to coat the surface of the body with porous materials. Several experimental investigations of this technology have been carried out in the last decade. A first study on the effectiveness of porous coatings was performed by Sueki *et al.* [1], who demonstrated that porosity affects the flow past the cylinder by depriving momentum of the wake region and suppressing the unsteady motion of the shed vortices. Comparable results were obtained for cylinders coated with metal foam by Aguiar *et al.* [2], who also observed a reduction in pressure drag due to the penetration of flow within the inner volume. Moreover, Geyer *et al.* [3] tested several porous media for the covers and showed that materials that are highly permeable to air yield the best noise-mitigation performance. An analogous study was carried out by Showkat Ali *et al.* [4], who highlighted that the most striking effect of the porous treatment of the cylinder on the flow field is to shift the vortex-formation region downstream and decrease the turbulence kinetic energy. In this case, an increase in drag was found due to the widening of the wake region and the lower velocities downstream of the body. Xia *et al.* [5] applied proper orthogonal decomposition to particle image velocimetry (PIV) measurements of a cylinder coated with metal foam and suggested that the larger vortex-formation length is caused by the weakened interactions between the shear layers. Furthermore, Sadeghipour *et al.* [6] observed that the distance from the surface at which the vortex shedding starts is directly linked to the permeability of the coating material. The important role played by this parameter on the wake-flow stabilization was also confirmed by Geyer [7].

*Postdoctoral Researcher, Department of Aerodynamics, Wind Energy, Flight Performance and Propulsion, r.zamponi@tudelft.nl, AIAA Member
†Assistant Professor, Department of Aerodynamics, Wind Energy, Flight Performance and Propulsion, f.avallone@tudelft.nl, AIAA Member
‡Associate Professor, Department of Aerodynamics, Wind Energy, Flight Performance and Propulsion, d.ragni@tudelft.nl, AIAA Member
§Professor Emeritus, Department of Novel Aerospace Materials, S.vanderZwaag@tudelft.nl, AIAA Member

All the above studies establish the potential of a porous treatment of the cylinder as an aerodynamic-sound-mitigation strategy. However, the definitive link between the alterations in the flow field and the noise attenuation has not been clarified yet. The research work presented in the manuscript aims to shed light upon this connection and elucidate the noise-reduction mechanisms associated with a porous coating of the cylinder. Indeed, an improved understanding of how the generated sound sources are affected by porosity can be instrumental in designing optimized and more efficient solutions. An experimental campaign has been carried out at the A-Tunnel facility of the Delft University of Technology (TUD) to pursue this objective. Far-field acoustic measurements have been performed on circular cylinders coated with metal foam to evaluate the noise-mitigation performance of this technology, whereas the location where the noise sources are distributed has been characterized through acoustic beamforming. The statistics of the wake-flow region of the cylinder have been determined using PIV to analyze the changes in the turbulent field due to porosity.

The manuscript is structured as follows. The measurement setup arranged for the experimental campaign is described in Section II. In Section III, the main results are outlined and discussed, highlighting the connection between the stabilization of the wake-flow region and the noise attenuation provided by the porous coating. Finally, the conclusions are drawn in Section IV.



## II. Methodology

### A. Wind-tunnel facility and cylinder specimen

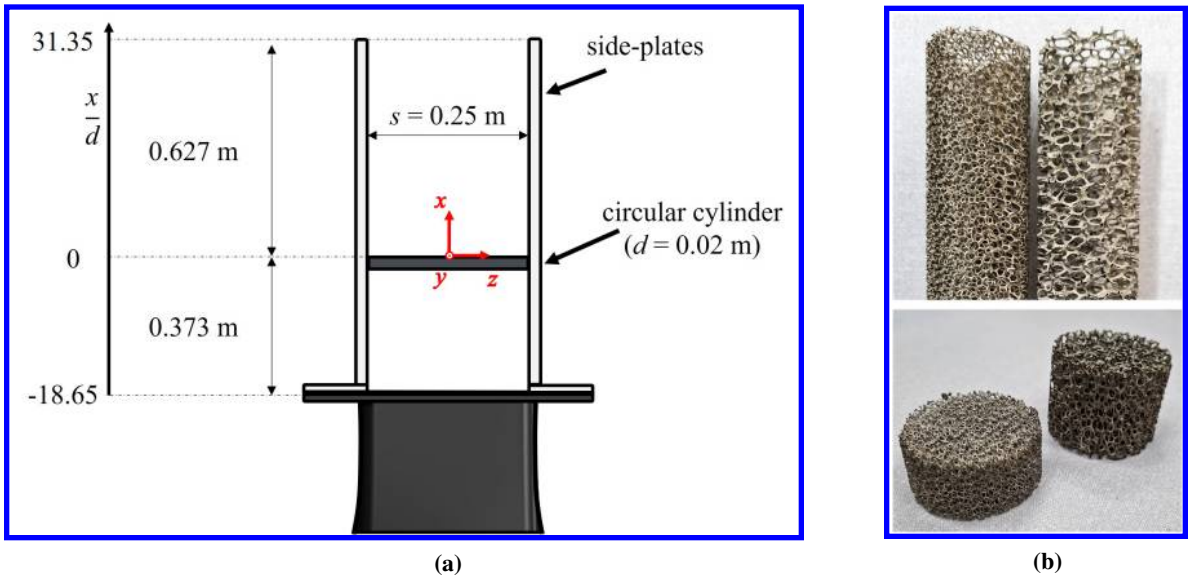


**Fig. 1 (a) Test section showing the outlet nozzle, side plates, and cylinder specimen, including the reference system considered for the presentation of the results. (b) Picture of the two metal-foam coatings used in the measurement campaign (at the top) and samples employed to characterize the porous medium (at the bottom).**

The experiments presented in this paper have been performed at the A-tunnel facility of the TUD. This is a vertical open–jet wind tunnel located in an anechoic chamber that is equipped with Flamex Basic acoustic absorbing foam and defined by a cutoff frequency of 250 Hz. A detailed description of its design and main features is provided by Merino-Martínez *et al.* [8]. The outlet nozzle of the wind tunnel is flush-mounted at the exit of the contraction. It has a height of 1 m and features a rectangular exit plane with a contraction ratio of 42 to 1, a span of $s = 0.250$ m, and a width of $w = 0.400$ m. Two side plates guide the flow from the outlet nozzle and support the cylinder specimens having a length equal to $s$. A sketch of the setup is depicted in Fig. 1a, where the reference system adopted for the presentation of the results is also indicated. In particular, the $x$-axis is aligned with the flow direction, the $z$-axis is aligned with the spanwise direction of the body, and the $y$-axis is oriented in the normal direction to form a right-handed coordinate system. The origin is set at the midspan of the cylinder's trailing edge.

Three cylinder configurations have been tested: a bare cylinder, or baseline, and two cylinders covered with porous materials characterized by different properties, as will be explained in Section II.B. The diameter $d$ of the inner cylinder

has been kept constant to model a scenario in which external material is integrated into an existing device. The outer diameter $D$ of the coated cylinder is therefore determined by the thickness of the cover $t$, according to $D = d + 2t$. The geometry of the specimens has been subsequently designed to meet the following criteria: i) the aspect ratio of the cylinder, i.e., the ratio of the length to the diameter, should be larger than 7 to allow the vortex shedding to occur [9]; ii) the cylinder diameter should be sufficiently small to minimize the blockage exerted by the body; iii) the vortex-shedding frequency $f_{VS}$, determined by $f_{VS} \approx 0.2\,U_\infty/d$, $U_\infty$ being the free-stream flow velocity, should be above the cutoff frequency of the anechoic facility; iv) $D$ should be high enough to make it possible to integrate the porous coating; v) $t$ should be large enough for the flow to penetrate the porous medium. The resulting dimensions have been $d = 20$ mm, $D = 30$ mm, and $t = 5$ mm, leading to aspect ratios of $L/d = 12.5$ and $L/D = 8.33$.

The measurements have been carried out at free-stream flow velocities in the subcritical regime ranging from $U_\infty = 25\,\mathrm{m\,s^{-1}}$ to $U_\infty = 70\,\mathrm{m\,s^{-1}}$, which correspond to Reynolds numbers based on the inner cylinder diameter of $Re_d = 3.4 \times 10^4$ and $Re_d = 9.5 \times 10^4$, respectively. The flow velocity is measured through a Pitot static tube connected to a Mensor DPG 2400 pressure gauge and featuring accuracy of 0.03 % of the read value. The full qualification of the outlet nozzle has been already performed by Merino-Martínez *et al.* [8], who found that the mean velocity in the streamwise direction was uniform within 0.6 % independently of the free-stream velocity, whereas the turbulence intensity of the clean flow was below 0.1 % for the entire range of operative velocities.



### B. Porous coatings

The porous coatings are made of two different types of Nickel Ni open-cell metal foams manufactured through the electrodeposition of pure Nickel on a polyurethane foam, which resulted in a homogeneous microstructure based on a dodecahedron-shaped cell. This material has been already employed for similar experimental campaigns reported in the literature [1, 2, 10]. The two metal foams feature a nominal cell diameter of 10 PPI and 30 PPI, where PPI is a non-SI unit typically used as an index for the number of pores per inch, and a porosity $\varphi$, defined as the ratio of the void volume to the total volume, of 80 % and 95 %, respectively. These values have been chosen in agreement with the literature results mentioned in Section I. A picture of the two materials is visible in Fig. 1b.

The characterization of the porous media has been carried out using the experimental rig designed by Rubio Carpio *et al.* [11]. This method consists of least-squares fitting the Hazen-Dupuit-Darcy quadratic equation [12]

$$\frac{\Delta p}{t_s} = \frac{\mu}{K} v_d + \rho C v_d^2, \tag{1}$$

where $\Delta p$ is the pressure drop across a homogeneous porous material sample with thickness $t_s$, $\mu$ is the fluid dynamic viscosity, $v_d$ is the Darcian velocity, which is determined as the ratio of the volumetric flow rate to the cross-section area of the material sample, and $K$ and $C$ are the static permeability and form coefficient of the porous medium, which account for pressure losses due to viscous and inertial effects, respectively. The term $R = \Delta p/(t_s\, v_d)$ also denotes the static air-flow resistivity of the material. A total of 20 values of pressure drop, corresponding to Darcian velocities ranging between $0\,\mathrm{m\,s^{-1}}$ and $2.5\,\mathrm{m\,s^{-1}}$, are employed for fitting Eq. (1).

Two pressure ports are located 50 mm upstream and downstream of the test section and are connected to a Mensor DPG 2101 pressure gauge having an accuracy of 2 Pa. The volumetric flow rate is controlled through an Aventics pressure regulator and evaluated by a TSI 4040 volumetric flow meter that is placed upstream of the pipe and features an accuracy of 2 % of the read value.

**Table 1 Measured properties for the two metal-foam samples. Quantities in parentheses refer to the nominal values provided by the manufacturer.**

| PPI [-] | $\varphi$ [%] | $R$ [N s m$^{-4}$] | $K$ [m$^2$] | $C$ [m$^{-1}$] |
|---|---|---|---|---|
| (30) | (80) | $1.296 \times 10^2$ | $1.390 \times 10^{-7}$ | $1.834 \times 10^2$ |
| (10) | (95) | $4.148 \times 10^1$ | $4.371 \times 10^{-7}$ | $1.103 \times 10^2$ |

The porous-material samples are 55 mm metal-foam disks (see Fig. 1b) inserted in a hollow aluminum cylinder that is located in the test section. A parametric study on $t_s$ has been performed to prevent the occurrence of entrance or exit effects on the measured pressure drop that may prevail if the thickness of the sample is too small [13, 14]. Therefore, $t_s$ has been varied between 25 mm and 100 mm and between 40 mm and 120 mm for the 30 PPI and 10 PPI metal foam,

respectively. Convergence in the values of $K$ and $C$ has been found for the thickest samples, suggesting that spurious effects can be considered negligible. The results of the characterization are listed in Table 1 and show that the larger the cell diameter of the porous medium is, the higher the static permeability and the lower the static air-flow resistivity and the form coefficient are.

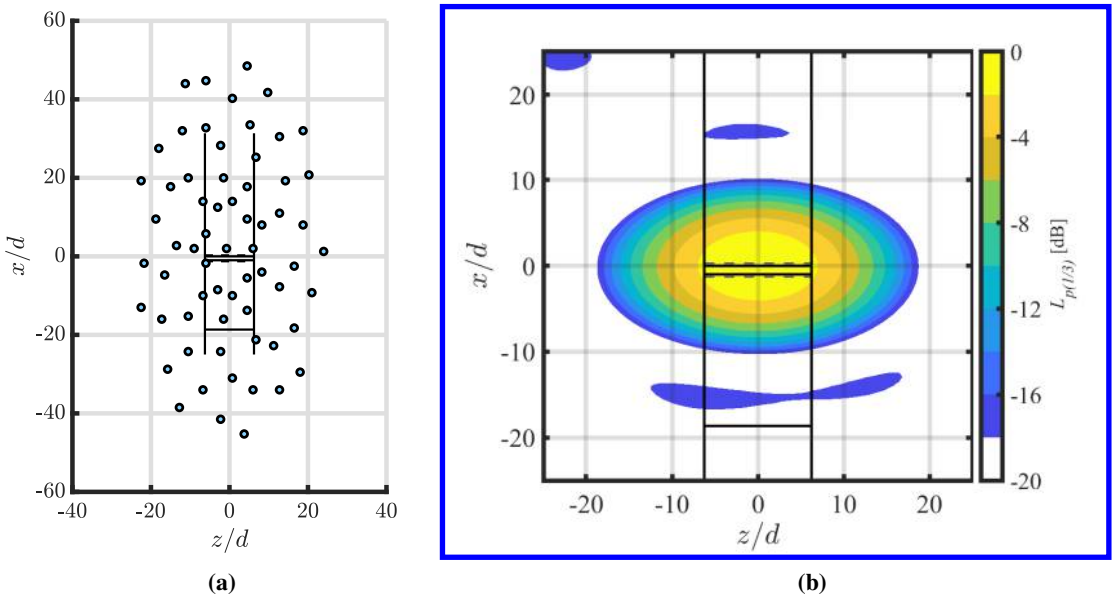


**Fig. 2 (a) Relative position of the microphone array and the test section. The black lines indicate side-plates, nozzle exit, and cylinder leading edge and trailing edge. (b) Point-spread function at $f_{1/3} = 1.25$ kHz for a simulated source emitting white noise at the origin of the coordinate system. The flow goes from the bottom to the top of the maps.**

### C. Far-field acoustic measurements

A microphone array consisting of 64 G.R.A.S. 40 PH analog free-field microphones with integrated constant-current power amplifiers is employed for the far-field acoustic measurements. Each microphone features a diameter of 0.007 mm and a length of 0.059 mm, and is characterized by a flat frequency response within ±1 dB from 50 Hz to 5 kHz and within ±2 dB from 5 kHz to 20 kHz. The transducers are connected to a data acquisition system consisting of 4 NI PXIe-4499 Sound and Vibration Modules having a 24 bits resolution and a 204.8 kHz maximum sampling rate. The boards are controlled by a NI RMC-8354 computer via a NI PXIe-8370 board. All the microphones are calibrated in amplitude using a G.R.A.S. 42AG pistonphone, which emits a sinusoidal wave of 94 dB at 1 kHz.

The array has an aperture of approximately 2 m and is arranged in an optimized multiarm spiral configuration [15] placed parallel to the $x - z$ plane. With respect to the reference system introduced in Section II.A, the central microphone is placed at $(x,\ y,\ z) = (2\,d,\ 50\,d,\ -0.75\,d)$. A sketch of the relative position of the microphone array and the test section is illustrated in Fig. 2a. For each cylinder configuration, data have been acquired at a sampling frequency of 102.4 kHz for 20 s. 7 free-stream Reynolds numbers have been considered, namely $Re_d = 3.4 \times 10^4,\ 4.1 \times 10^4,\ 4.8 \times 10^4,\ 5.4 \times 10^4,\ 6.8 \times 10^4,\ 8.2 \times 10^4$ and $9.5 \times 10^4$.

The power spectra of the measured acoustic signals have been computed using the Welch method [16], with blocks of $1 \times 2^{13}$ samples windowed through a Hanning weighting function having a 50 % data overlap, thus delivering a frequency resolution of 12.5 Hz. Moreover, to provide a visualization of the noise sources, the data have been subsequently post-processed by means of an in-house generalized inverse beamforming (GIBF) technique validated through numerical and experimental benchmark datasets [17–19]. For more information on the method, the reader is referred to [20].

The scanning grid for the evaluation of the potential sources ranges between $-25 < z/d < 25$ and $-25 < x/d < 25$, with a spatial resolution of $0.5\,d$, and is centered at the origin of the reference system. The extension of the grid can be observed in Fig. 2b, which shows the point-spread function (PSF) [21] of the array for a simulated point source placed at the origin and emitting white noise at the one-third-octave frequency band of $f_{1/3} = 1.25$ kHz. As can be

seen from this sound map, the PSF features axial symmetry with respect to the $x$ and $z$ axes and is characterized by a higher resolution along $x$, making the array suitable to separate noise sources in the streamwise direction. Furthermore, corrections to account for the convection of the mean flow and refraction of the shear layer have been applied following the method proposed by Sijtsma [22], whereas measurements of the test section without the cylinder specimens have been taken to evaluate the background noise of the facility.

### D. PIV measurements

Two-component (2C) PIV experiments have been performed on a $x - y$ plane at the midspan of the cylinder, centered in the wake region of the body. Two LaVision Imager sCMOS camera having a sensor of 2560 px × 2160 px and pixel pitch of 6.5 µm and equipped with Nikon NIKKOR 105 mm focal-distance macro-objectives set at $f_\# = 11$ have been placed at approximately 75 $d$ from the measurement plane. Scheimpflug adapters have been installed on each camera to account for misalignment angles minor than 5°. Seeding has been produced by a SAFEX Twin-Fog Double Power fog generator with a SAFEX Long-Lasting glycol mix. The particles, whose generated mean drop diameter is estimated to be 0.5 µm, have been introduced in the wind-tunnel circuit to grant a uniform concentration while recirculating in the test section. The laser sheet has been obtained through laser pulses with a wavelength of 532 nm and energy of 200 µJ per pulse that are generated by a Quantel Evergreen EVG00200 double-pulse Nd:YAG system, resulting in an approximate thickness of 1 mm.

Sets of 2000 uncorrelated image pairs have been acquired at a sampling frequency of 10 Hz for each cylinder configuration at free-stream Reynolds numbers of $Re_d = 4.1 \times 10^4$, $Re_d = 5.4 \times 10^4$, and $Re_d = 6.8 \times 10^4$. The combined field of view (FOV) has a dimension of 8.1 $d$ × 13.2 $d$ and a digital resolution of 13.9 px mm$^{-1}$ (magnification factor: 0.087).

The processing of the raw images is carried out with the commercial software LaVision Davis 10.1.2 employing a multi-pass cross-correlation approach [23] with a final interrogation window of 16 px × 16 px and 75 % overlapping, which lead to a spatial resolution of 0.06 $d$ × 0.06 $d$ and a vector spacing of 0.015 $d$ × 0.015 $d$. The separation time between two frames has been adapted to maintain a pixel displacement in the free-stream of about 12 px.

The overall systematic and random components of PIV uncertainty can be determined with a method based on correlation statistics that evaluates the differences in the correlation peaks computed from a pair of interrogation windows mapped back onto each other [24]. The uncertainty is provided for individual instantaneous velocity vectors and is quantified through statistical techniques [25]. The results indicate a maximum uncertainty on the mean-velocity magnitude below 0.02 $U_\infty$ for all the Reynolds numbers considered in the study. For the processing of the results, the set of 2000 snapshots has been ensemble-averaged at each location of the measurement domain to retrieve the statistics of the flow field.

## III. Results and discussion

### A. Aeroacoustic results

The sound-pressure levels $L_p$ of the signal measured by the central microphone of the array are reported in Fig. 3 for the three cylinder configurations and different free-stream Reynolds numbers. The results are presented in function of the Strouhal number based on $d$ and $U_\infty$. In general, the porous coatings are effective in reducing noise, with a trend that is independent of the flow velocity. The difference in the outer diameter of the coated cylinder results in a shift of the tonal peak associated with the vortex shedding at $St = 0.185$ towards lower frequencies and a significant suppression of its amplitude, with peak-to-peak reductions of up to 30 dB. The Strouhal number linked to the vortex shedding for the baseline agrees with previous measurements involving circular cylinders tested in the same experimental setup [26]. An equivalent value would be retrieved for the 30 PPI coating if the acoustic spectra were scaled using $D = 0.03$ m, whereas a cylinder diameter of $D = 0.028$ m would be required to achieve the same result for the 10 PPI one. Indeed, the high static permeability of the latter configuration most likely changes the effective diameter of the cover, influencing the flow penetration. In addition, the 30 PPI metal foam seems to be more efficient in suppressing the vortex-shedding peak, whereas the 10 PPI one better mitigates its first harmonic. Interestingly, the sound pressure levels measured at the first-harmonic frequency for the 30 PPI case exceed those at the fundamental vortex-shedding frequency. This behavior was previously observed by Arcondoulis and Liu [27], but no definitive explanation for it has been found yet.

Two different trends define the broadband-noise range. On the one hand, for $St < 1$, a significant attenuation of up to 10 dB is found, and no clear distinction can be observed between the two metal foams. This result supports a scenario in

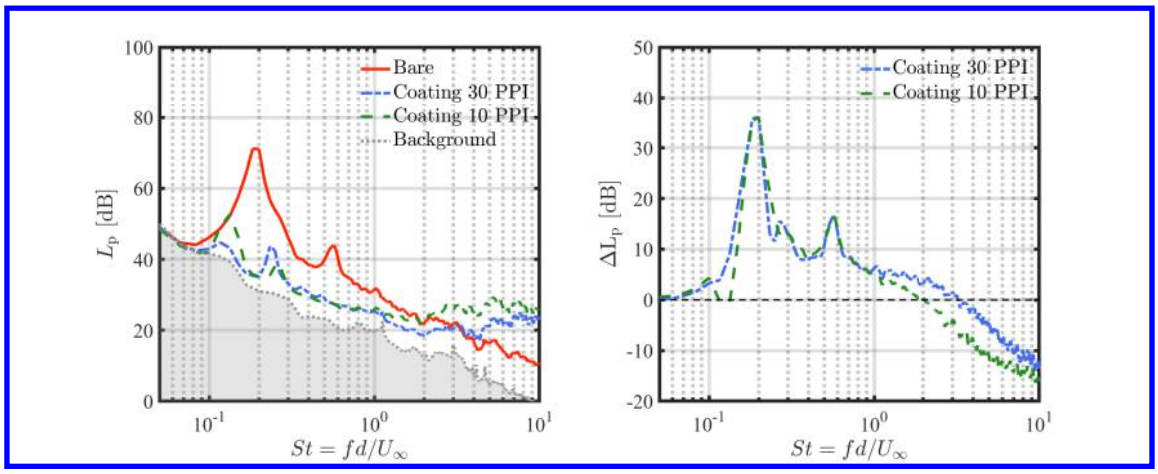


**(a)**

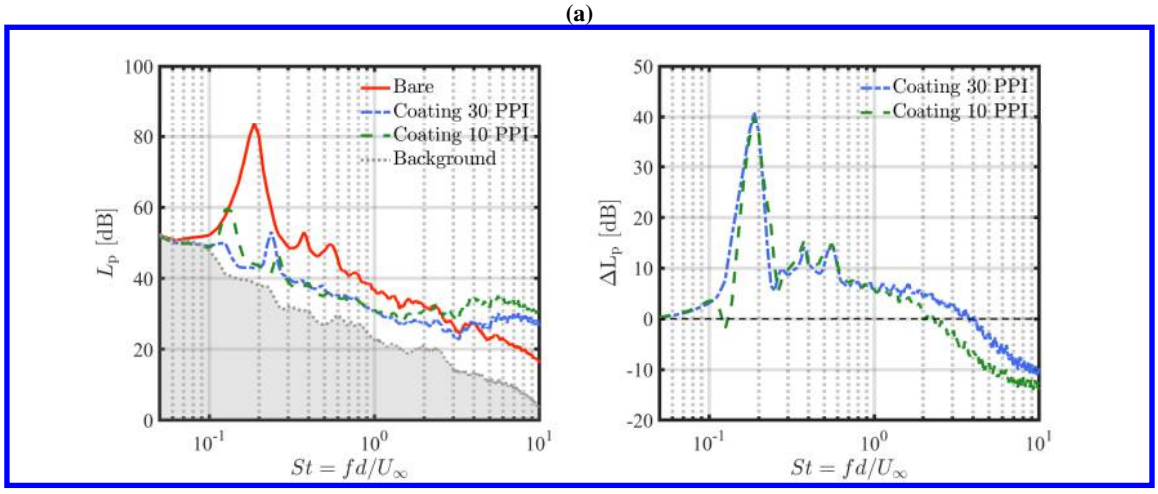


**(b)**

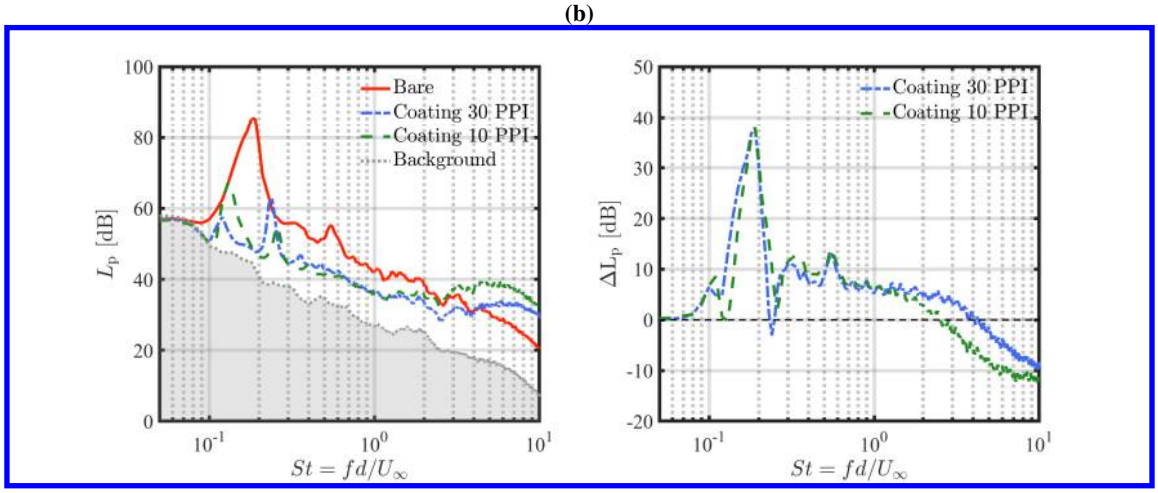


**(c)**

**Fig. 3 Absolute (on the left) and relative (on the right) sound pressure levels for the three cylinder configurations at (a) $Re_d = 4.1 \times 10^4$, (b) $Re_d = 5.4 \times 10^4$, and (c) $Re_d = 6.8 \times 10^4$ measured by the central microphone of the array and computed with a reference pressure of $p_{ref} = 20\,\mu$Pa. The dashed lines on the right indicate the tradeoff between increase and decrease in noise with respect to the baseline.**

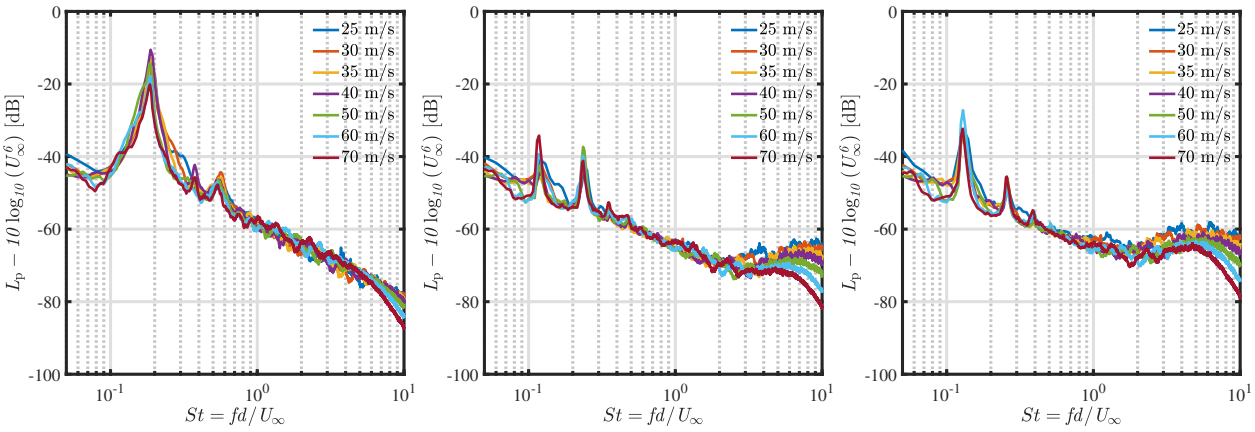


**Fig. 4 Sound pressure levels at different free-stream flow velocities for (a) the baseline and the cylinders coated with the (b)** 30 PPI **and (c)** 10 PPI **metal foams measured by the central microphone of the array and computed with a reference pressure of** $p_{\mathbf{ref}} = 20\,\mu$**Pa. The spectra are scaled with the sixth power of the flow velocity.**

which the sound-reduction mechanism acting in such a frequency range is not directly linked to the permeability of the porous material. On the other hand, for $St > 1$, the coated configurations start diverging, likely due to the effect of surface-roughness noise, which is more relevant and occurs at lower frequencies for the most permeable metal foam. This phenomenon is caused by the larger pore size that produces stronger coherent cavity modes where the incident flow permeates the medium, lowering the aeroacoustic performance of the porous treatment at higher frequencies with noise increments of up to 10 dB.

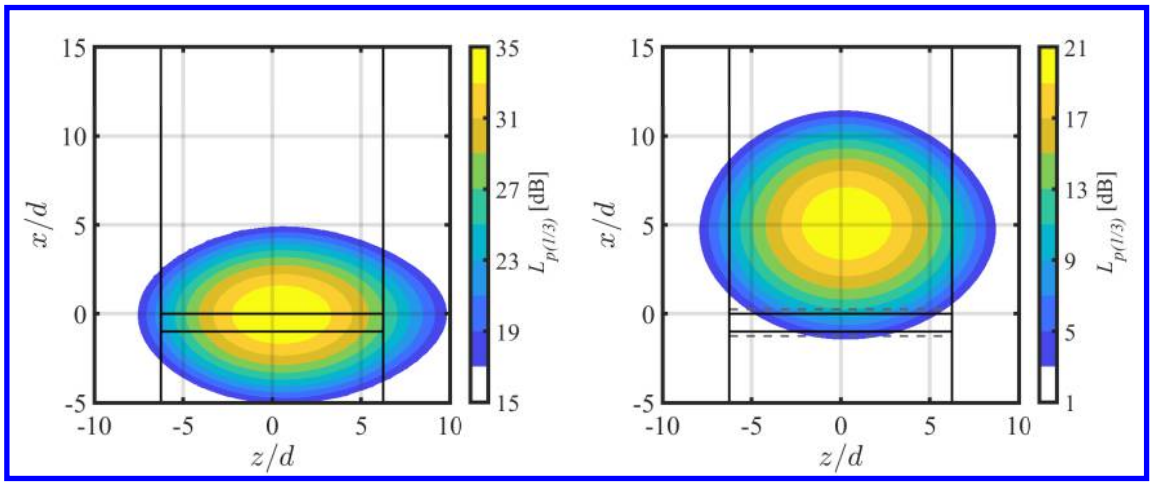


**Fig. 5 GIBF source-distribution maps for (a) the baseline and (b) the cylinder coated with the** 30 PPI **metal foam at** $f_{1/3} = 1.25$ kHz **and** $Re_d = 6.8 \times 10^4$ **(**$St = 0.5$**) computed with a reference pressure of** $p_{\mathbf{ref}} = 20\,\mu$**Pa.**

The scaling of $L_p$ with the flow velocity can shed light upon the nature of the generated sound sources. In Fig. 4, the sound-pressure levels are scaled with the sixth power of $U_\infty$, which is typically associated with a dipolar source [28]. In this case, a satisfactory collapse of the spectra is obtained for all the three cylinder configurations up to $St \approx 2$, in agreement with the literature findings [29]. However, the lack of collapse at higher Strouhal numbers implies that the noise-production mechanism for this frequency range is different, confirming the connection with the surface roughness indicated above.

The origin of the dipolar noise sources can be further analyzed using acoustic beamforming. GIBF source-distribution

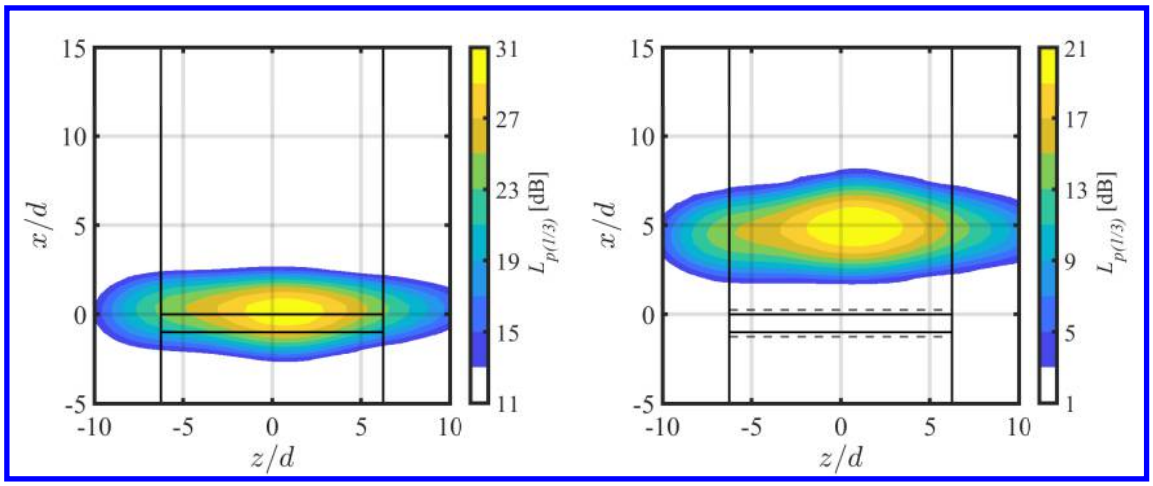


**(a)** **(b)**

**Fig. 6 GIBF source-distribution maps for (a) the baseline and (b) the cylinder coated with the** 30 PPI **metal foam at** $f_{1/3} = 2.5$ kHz **and** $Re_d = 6.8 \times 10^4$ ($St = 1$) **computed with a reference pressure of** $p_{\mathrm{ref}} = 20$ µPa**.**

maps at different one-third-octave frequency bands are illustrated in Figs. 5 to 7. The results for the baseline and the cylinder cylinder coated with the 30 PPI metal foam are presented for $Re_d = 6.8 \times 10^4$, but the discussions presented below can be generalized also to the other free-stream flow velocities. It is important to point out that inverse beamforming methods such as GIBF display the source-distribution contours instead of the peak-source intensity, differently from direct techniques [30]. Hence, the integration of the maps is required to assess the actual source strength, which explains the relatively low noise levels displayed in the plots.

Overall, the maps for the baseline feature higher $L_p$ than for the coated cylinders, in agreement with what has been observed in Fig. 3. At $f_{1/3} = 1.25$ kHz (Fig. 5), corresponding to $St = 0.5$, the dominant noise sources for the baseline are found in proximity of the trailing edge. Interestingly, those for the coated configuration are shifted more downstream. This finding suggests that the dipoles are not generated on the surface by a fluctuating reaction force, as in the classical view provided by Curle's analogy [28], but may be a consequence of the diffraction of a quadrupole located in the flow by the cylinder, which, for compact sources, is characterized by a dipolar nature [31]. More analyses will be required to clarify the present result, which will certainly be a topic for future work.

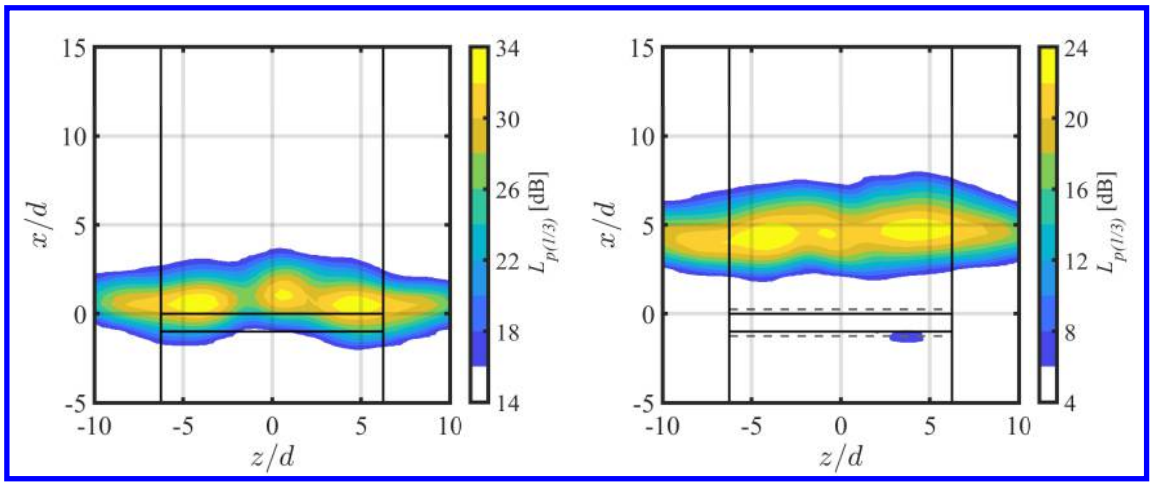


**(a)** **(b)**

**Fig. 7 GIBF source-distribution maps for (a) the baseline and (b) the cylinder coated with the** 30 PPI **metal foam at** $f_{1/3} = 5$ kHz **and** $Re_d = 6.8 \times 10^4$ ($St = 2$) **computed with a reference pressure of** $p_{\mathrm{ref}} = 20$ µPa**.**

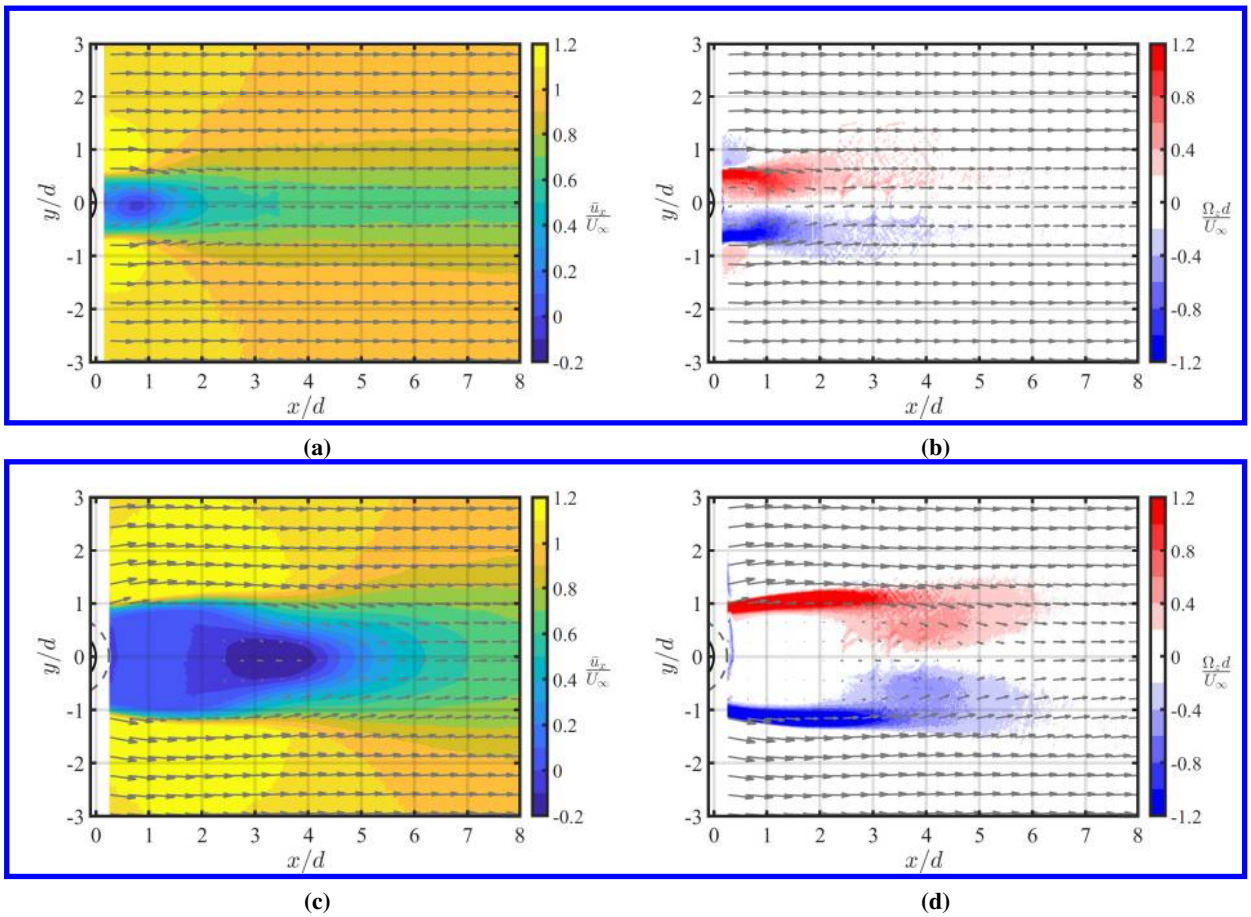


**Fig. 8 Normalized flow statistics for the bare cylinder (top row) and the cylinder coated with the** 30 PPI **(bottom row) metal foam measured at $Re_d = 6.8 \times 10^4$: (a)-(c) mean streamwise velocity; (b)-(d) mean spanwise vorticity. The gray arrows indicate the mean-flow streamlines.**

The same conclusions can be drawn for $f_{1/3} = 2.5$ kHz (Fig. 6), corresponding to $St = 1$. In this case, the source regions exhibit a more defined distributed nature in the spanwise direction thanks to the higher spatial resolution of the beamforming method at increased frequencies. The position of the dominant noise sources for the different configurations is consistent with the previous case, suggesting that the physical mechanisms at the basis of the downstream source shift are independent of the frequency.

Finally, at $f_{1/3} = 5$ kHz (Fig. 7), corresponding to $St = 2$, the dominant noise sources are still distributed along the span in the vicinity of the trailing edge and at $x/d \approx 5$ for the baseline and the 30 PPI case, respectively. It has been observed that this downstream source shift occurs for all those frequencies that are not dominated by surface roughness noise.

### B. Aerodynamic results

The study of the flow-field alterations due to porosity can elucidate the outcome of the aeroacoustic analysis conducted above. The mean streamwise velocity $\overline{u}_x$, mean spanwise vorticity $\Omega_z$, different components of the Reynolds-stress tensor defined as $\tau'_{ij} = \overline{u'_i u'_j}$, and turbulence kinetic energy $k = 0.5\,(\overline{u'_x} + \overline{u'_y})$ are shown in Figs. 8 to 10 for the baseline and the cylinder coated with the 30 PPI metal foam. All the values are normalized with $U_\infty$ and/or $d$. Also in this case, the results are presented for $Re_d = 6.8 \times 10^4$, but equivalent considerations can be extended to the other free-stream Reynolds numbers.

As introduced in Section I, the most striking effect of the porous coating on the velocity field is to widen the cylinder wake, reinjecting low-energy fluid past the body, and stabilize the flow. As a consequence, the recirculation zone in the

wake, located close to the body surface for the baseline (Fig. 8a), moves further downstream for the coated configuration (Fig. 8c). This trend is expected to be less emphasized for the 10 PPI metal foam. Indeed, the higher static permeability of the latter coating results in a more substantial flow penetration within the porous medium [32] that, in turn, reduces the low-energy flow region in the near wake and limits the related increment in vortex-formation length. Such an effect is emphasized by the decrease in the effective cylinder diameter mentioned in Section III.A.

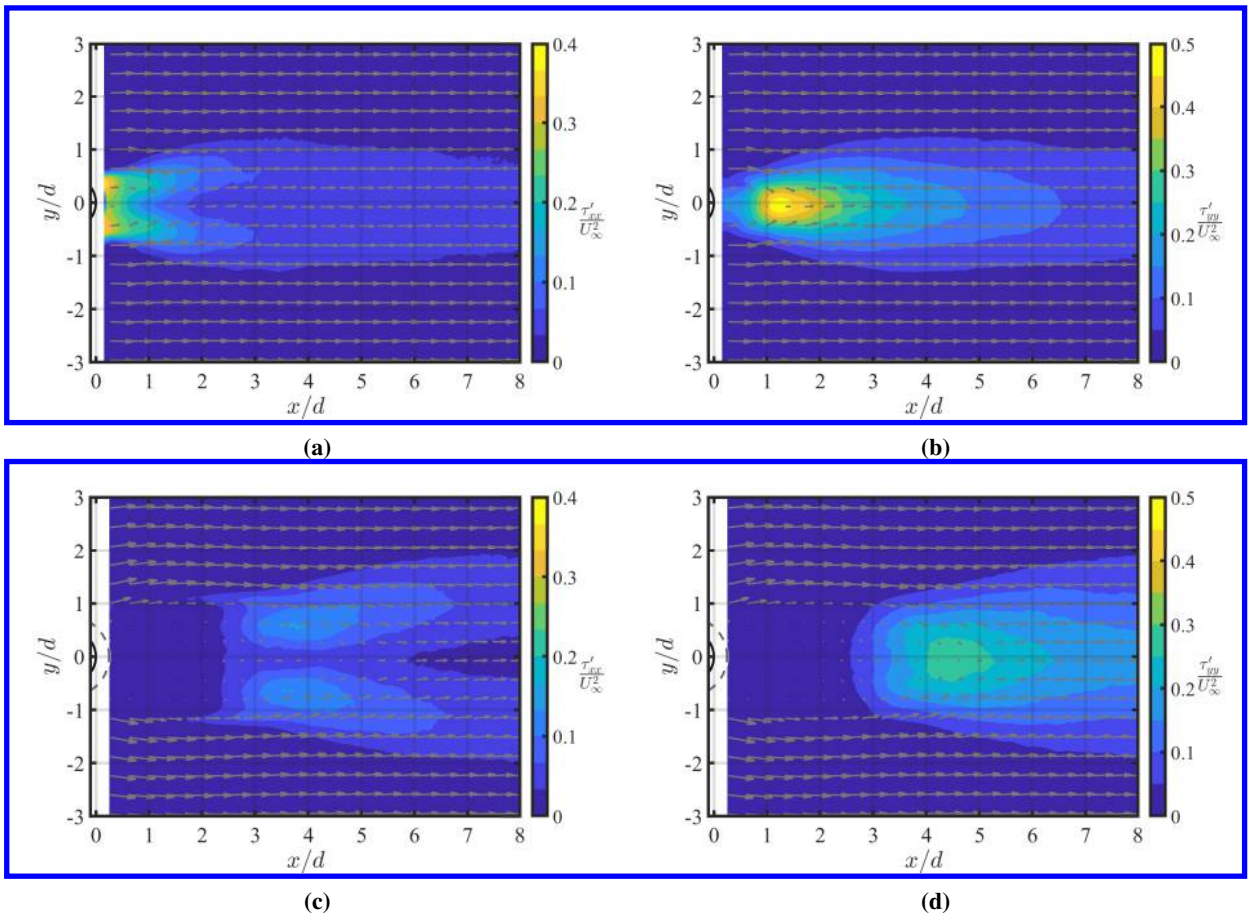


**Fig. 9 Normalized flow statistics for the bare cylinder (top row) and the cylinder coated with the** 30 PPI **(bottom row) metal foam measured at** $Re_d = 6.8 \times 10^4$**: (a)-(c) component** $\tau'_{xx}$ **of the Reynolds stress tensor; (b)-(d) component** $\tau'_{yy}$ **of the Reynolds stress tensor. The gray arrows indicate the mean-flow streamlines.**

Downstream of the recirculation zone, the periodic shedding of the vortical structures begins. This phenomenon can be observed from the mean-spanwise-vorticity contours: for the baseline (Fig. 8b), the regions of maximum and minimum $\Omega_z$ are spread over an area close to the cylinder surface, up to $x/d \approx 2$. When the 30 PPI coating is installed (Fig. 8d), the mean-spanwise-vorticity field features thin shear layers delimiting the wake that start expanding from $x/d \approx 4$ on, in correspondence with the recirculation zones. The transition between these two regions denotes the vortex-formation length.

In addition, the porous coating has a strong effect on the evolution of the Reynolds stresses in the wake, in agreement with the literature results reviewed in Section I. Besides providing a more detailed view of the turbulent flow induced by the vortex shedding, the study of the different components of the Reynolds-stress tensor can also shed light upon the quadrupolar sound sources produced as a result of unsteady convection of flow. Indeed, for high Reynolds numbers, the contribution of the viscous forces can be neglected and, with the assumption of incompressible and isentropic flow, Lighthill's stress tensor can be approximated as $T_{ij} \approx \rho u_i u_j$ [33]. As mentioned in Section III.A, these sources may play an important role in the radiated far-field noise.

Overall, the porous treatment of the circular cylinder has the twofold effect of reducing the amplitude of the Reynolds stresses and moving the region where turbulence is generated more downstream. In particular, the streamwise Reynolds

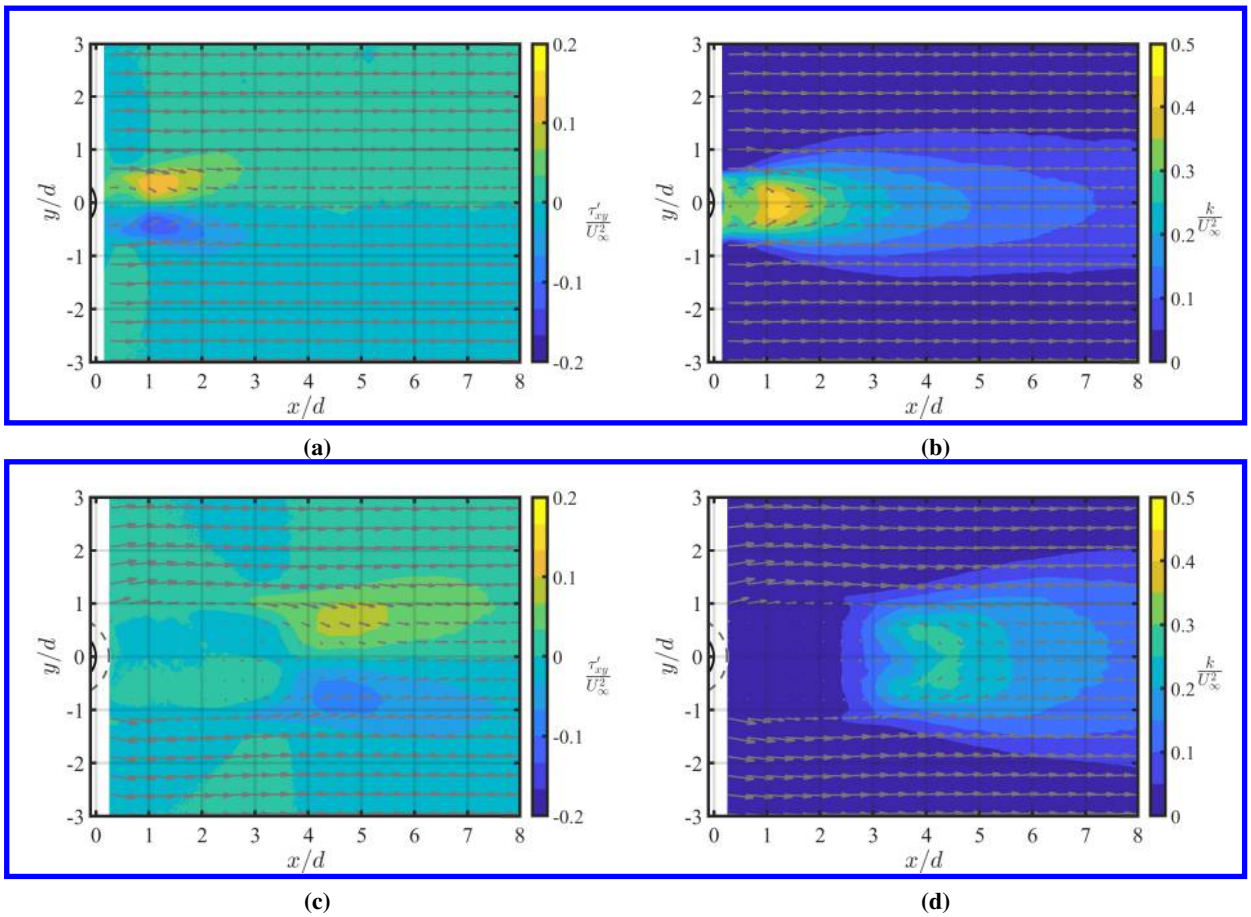


**Fig. 10 Normalized flow statistics for the bare cylinder (top row) and the cylinder coated with the** 30 PPI **(bottom row) metal foam measured at** $Re_d = 6.8 \times 10^4$**: (a)-(c) component** $\tau'_{xy}$ **of the Reynolds stress tensor; (b)-(d) turbulence kinetic energy. The gray arrows indicate the mean-flow streamlines.**

stresses $\tau'_{uu}$ (Figs. 9a and 9c) are the most affected by porous cover. These components of the stress tensor are related to the flow recirculation and get significantly attenuated when the recirculation zone is shifted farther from the surface. On the other hand, the crosswise Reynolds stresses $\tau'_{vv}$ (Figs. 9b and 9d) are associated with the oscillatory movement of the turbulent structures and are maximum at the location when the vortex shedding begins. Likewise, they are substantially reduced by the porous treatment of the body. Furthermore, similar observations can be made for the components $\tau'_{uv}$ of the Reynolds-stress tensor (Figs. 10a and 10c), even though their magnitude is considerably lower than that of the other components previously analyzed.

In view of the above, the flow statistical parameter that better summarizes the impact of the porous coating on the turbulent-flow field is the turbulence kinetic energy $k$ (Figs. 10b and 10d), which is mainly dominated by $\tau'_{vv}$, and, consequently, is maximum at the position where the vortex shedding is triggered. In this case, the reduction in the peak of $k$ amounts to approximately 45 %.

Finally, The outcome of the aeroacoustic and the aerodynamic analyses reported above hints at a link between the noise suppression due to the coating and the increase in vortex-formation length. Such a connection becomes more evident when the $k$ contours in Figs. 10b and 10d are compared with the GIBF sound-distribution maps in Figs. 5 to 7. For the bare cylinder, the dominant noise sources are distributed over the body's trailing edge, i.e., slightly upstream of the peak region of the turbulence kinetic energy. In contrast, the dominant noise sources for the coated cylinder are located in the area where the turbulent structures begin their oscillatory movement. It has been observed that this connection is valid for all the frequencies for which surface-roughness noise does not dominate.

## IV. Concluding remarks

The present research work investigates the link between the stabilization of the flow downstream of a circular cylinder coated with porous materials and the corresponding aerodynamic-noise reduction. This objective has been pursued by combining sound-source and flow-field visualization techniques. The experimental results show that, for a coated configuration, the dominant noise sources lie in the flow, in a region downstream of the body that is determined by the vortex-formation length, and are defined by a dipolar directivity pattern. This finding does not agree with the common view associated with Curle's analogy, according to which the noise is produced by the fluctuating force that the cylinder exerts on the surrounding fluid, but may be explained by considering the effect of the sound diffraction of quadrupolar sources located in the wake flow.

In view of the above, it appears that the main noise-reduction mechanism linked to the porous treatment of circular cylinder is to move the dominant sound sources, which are produced by the onset of the vortex shedding, more downstream and lower their strength. Although additional studies will be required to further elucidate this mechanism, the outcomes of this research can provide guidelines for a more effective design of passive noise-control strategies. Maximizing the downstream source shift represents a valid design criterion for the treatment of a bluff body, which could be achieved with an optimization of the porous medium within the cover, exploiting the recent advancements in the additive-manufacturing techniques.



## Acknowledgements

This work is part of the IPER-MAN project (Innovative PERmeable Materials for Airfoil Noise Reduction), project number 15452, funded by The Netherlands Organization for Scientific Research (NWO).

## References

[1] Sueki, T., Takaishi, T., Ikeda, M., and Arai, N., "Application of porous material to reduce aerodynamic sound from bluff bodies," *Fluid Dynamics Research*, Vol. 42, No. 1, 2010, p. 015004. https://doi.org/10.1088/0169-5983/42/1/015004.

[2] Aguiar, J., Yao, H., and Liu, Y., "PASSIVE FLOW/NOISE CONTROL OF A CYLINDER USING METAL FOAM," *The 23rd International Congress on Sound and Vibration*, The International Institute of Acoustics and Vibration, 2016, p. 9.

[3] Geyer, T., and Sarradj, E., "Circular cylinders with soft porous cover for flow noise reduction," *Experiments in Fluids*, Vol. 57, No. 3, 2016, p. 30. https://doi.org/10.1007/s00348-016-2119-7.

[4] Showkat Ali, S., Liu, X., and Azarpeyvand, M., "Bluff Body Flow and Noise Control Using Porous Media," *22nd AIAA/CEAS Aeroacoustics Conference*, American Institute of Aeronautics and Astronautics, Lyon, France, 2016. https://doi.org/10.2514/6.2016-2754.

[5] Xia, C., Wei, Z., Yuan, H., Li, Q., and Yang, Z., "POD analysis of the wake behind a circular cylinder coated with porous media," *Journal of Visualization*, Vol. 21, No. 6, 2018, pp. 965–985. https://doi.org/10.1007/s12650-018-0511-5.

[6] Sadeghipour, S., Showkat Ali, S., Liu, X., Azarpeyvand, M., and Thorpe, G., "Control of flows around bluff bodies mediated by porous materials," *Experimental Thermal and Fluid Science*, Vol. 114, 2020, p. 110048. https://doi.org/10.1016/j.expthermflusci.2020.110048.

[7] Geyer, T., "Experimental evaluation of cylinder vortex shedding noise reduction using porous material," *Experiments in Fluids*, Vol. 61, No. 7, 2020, p. 153. https://doi.org/10.1007/s00348-020-02972-0.

[8] Merino-Martínez, R., Rubio Carpio, A., Lima Pereira, L., van Herk, S., Avallone, F., Ragni, D., and Kotsonis, M., "Aeroacoustic design and characterization of the 3D-printed, open-jet, anechoic wind tunnel of Delft University of Technology," *Applied Acoustics*, Vol. 170, 2020, p. 107504. https://doi.org/10.1016/j.apacoust.2020.107504.

[9] Porteous, R., Moreau, D., and Doolan, C., "A review of flow-induced noise from finite wall-mounted cylinders," *Journal of Fluids and Structures*, Vol. 51, 2014, pp. 240–254. https://doi.org/10.1016/j.jfluidstructs.2014.08.012.

[10] Arcondoulis, E., Liu, Y., Li, Z., Yang, Y., and Wang, Y., "Structured Porous Material Design for Passive Flow and Noise Control of Cylinders in Uniform Flow," *Materials*, Vol. 12, No. 18, 2019, p. 2905. https://doi.org/10.3390/ma12182905.

[11] Rubio Carpio, A., Merino Martínez, R., Avallone, F., Ragni, D., Snellen, M., and van der Zwaag, S., "Experimental characterization of the turbulent boundary layer over a porous trailing edge for noise abatement," *Journal of Sound and Vibration*, Vol. 443, 2019, pp. 537–558. https://doi.org/10.1016/j.jsv.2018.12.010.

[12] Ingham, D., and Pop, I., *Transport phenomena in porous media*, Elsevier, 1998. https://doi.org/10.1016/B978-0-08-042843-7.X5000-4.

[13] Baril, E., Mostafid, A., Lefebvre, L., and Medraj, M., "Experimental Demonstration of Entrance/Exit Effects on the Permeability Measurements of Porous Materials," *Advanced Engineering Materials*, Vol. 10, No. 9, 2008, pp. 889–894. https://doi.org/10.1002/adem.200800142.

[14] Dukhan, N., and Patel, K., "Effect of sample's length on flow properties of open-cell metal foam and pressure-drop correlations," *Journal of Porous Materials*, Vol. 18, No. 6, 2011, pp. 655–665. https://doi.org/10.1007/s10934-010-9423-z.

[15] Luesutthiviboon, S., Ragni, D., Avallone, F., and Snellen, M., "An alternative permeable topology design space for trailing-edge noise attenuation," *International Journal of Aeroacoustics*, Vol. 20, No. 3-4, 2021, pp. 221–253. https://doi.org/10.1177/1475472X211003295.

[16] Welch, P., "The use of fast Fourier transform for the estimation of power spectra: A method based on time averaging over short, modified periodograms," *IEEE Transactions on Audio and Electroacoustics*, Vol. 15, No. 2, 1967, pp. 70–73. https://doi.org/10.1109/TAU.1967.1161901.

[17] Zamponi, R., Van de Wyer, N., and Schram, C., "An Improved Regularization of the Generalized Inverse Beamforming Applied to a Benchmark Database," *7th Berlin Beamforming Conference*, BeBeC, Berlin, Germany, 2018.

[18] Merino-Martínez, R., Sijtsma, P., Rubio Carpio, A., Zamponi, R., Luesutthiviboon, S., Malgoezar, A., Snellen, M., Schram, C., and Simons, D., "Integration methods for distributed sound sources," *International Journal of Aeroacoustics*, Vol. 18, No. 4-5, 2019, pp. 444–469. https://doi.org/10.1177/1475472X19852945.

[19] Merino-Martínez, R., Luesutthiviboon, S., Zamponi, R., Rubio Carpio, A., Ragni, D., Sijtsma, P., Snellen, M., and Schram, C., "Assessment of the accuracy of microphone array methods for aeroacoustic measurements," *Journal of Sound and Vibration*, Vol. 470, 2020, p. 115176. https://doi.org/10.1016/j.jsv.2020.115176.

[20] Zamponi, R., "Investigation of turbulence-surface interaction noise mechanisms and their reduction using porous materials," Ph.D. thesis, Delft University of Technology, Apr. 2021. https://doi.org/10.4233/uuid:d332c7e3-87be-4ed6-aa71-e629ef77e07a.

[21] Allen, C., Blake, W., Dougherty, R., Lynch, D., Soderman, P., and Underbrink, J., *Aeroacoustic Measurements*, Springer Berlin Heidelberg, Berlin, Heidelberg, 2002. https://doi.org/10.1007/978-3-662-05058-3.

[22] Sijtsma, P., "Phased Array Beamforming Applied to Wind Tunnel And Fly-Over Tests," Tech. rep., National Aerospace Laboratory NLR, Oct. 2010.

[23] Scarano, F., and Riethmuller, M., "Advances in iterative multigrid PIV image processing," *Experiments in Fluids*, Vol. 29, No. 7, 2000, pp. S051–S060. https://doi.org/10.1007/s003480070007.

[24] Wieneke, B., "PIV uncertainty quantification from correlation statistics," *Measurement Science and Technology*, 2015, p. 11. https://doi.org/doi:10.1088/0957-0233/26/7/074002.

[25] Sciacchitano, A., and Wieneke, B., "PIV uncertainty propagation," *Measurement Science and Technology*, Vol. 27, No. 8, 2016, p. 084006. https://doi.org/10.1088/0957-0233/27/8/084006.

[26] Tamaro, S., Zamponi, R., Ragni, D., Teruna, C., and Schram, C., "Experimental investigation of turbulent coherent structures interacting with a porous airfoil," *Experiments in Fluids*, Vol. 62, 2021, p. 94. https://doi.org/10.1007/s00348-021-03170-2.

[27] Arcondoulis, E., and Liu, Y., "The Effect of Porosity on the Porous Coated Cylinder Diameter," *Acoustics 2018: Hear to Listen*, Australian Acoustical Society, Adelaide, Australia, 2018, p. 11.

[28] Curle, N., "The influence of solid boundaries upon aerodynamic sound," *Proceedings of the Royal Society of London. Series A. Mathematical and Physical Sciences*, Vol. 231, No. 1187, 1955, pp. 505–514. https://doi.org/10.1098/rspa.1955.0191.

[29] Blevins, R., "Review of sound induced by vortex shedding from cylinders," *Journal of Sound and Vibration*, Vol. 92, No. 4, 1984, pp. 455–470. https://doi.org/10/c8gtms.

[30] Zamponi, R., Satcunanathan, S., Moreau, S., Ragni, D., Meinke, M., Schröder, W., and Schram, C., "On the role of turbulence distortion on leading-edge noise reduction by means of porosity," *Journal of Sound and Vibration*, Vol. 485, 2020, p. 115561. https://doi.org/10.1016/j.jsv.2020.115561.

[31] Gloerfelt, X., Pérot, F., Bailly, C., and Juvé, D., "Flow-induced cylinder noise formulated as a diffraction problem for low Mach numbers," *Journal of Sound and Vibration*, Vol. 287, No. 1-2, 2005, pp. 129–151. https://doi.org/10.1016/j.jsv.2004.10.047.

[32] Zamponi, R., Moreau, S., and Schram, C., "Rapid distortion theory of turbulent flow around a porous cylinder," *Journal of Fluid Mechanics*, Vol. 915, 2021, p. A27. https://doi.org/10.1017/jfm.2021.8.

[33] Lighthill, M., "On sound generated aerodynamically I. General theory," *Proceedings of the Royal Society of London. Series A. Mathematical and Physical Sciences*, Vol. 211, No. 1107, 1952, pp. 564–587. https://doi.org/10.1098/rspa.1952.0060.